Available online at www.sciencedirect.com

ScienceDirect

Procedia CIRP 124 (2024) 741–745

www.elsevier.com/locate/procedia

13th CIRP Conference on Photonic Technologies [LANE 2024], 15-19 September 2024, Fürth, Germany

Laser power density distribution metrology to support emerging trends in metal Additive Manufacturing

David Deisenroth[a]*, Sergey Mekhontsev[a], Jordan Weaver[a], and Samantha Webster[b]

[a]National Institute of Standards and Technology, Engineering Laboratory, 100 Bureau Dr., Gaithersburg, MD 20899, USA
[b]National Institute of Standards and Technology, Materials Measurement Laboratory, 100 Bureau Dr., Gaithersburg, MD 20899, USA

* Corresponding author. Tel.: +1-301-975-2594. *E-mail address:* david.deisenroth@nist.gov

Abstract

The laser power density distribution (PDD) applied to a material is a predominant process parameter that directly affects the properties of parts that are built with metal additive manufacturing (AM). Despite its prevalent effect on melting (especially melting depth and cooling rate), accurate characterization of PDDs in metal AM has been largely inadequate because of the challenging nature of such measurements. The metrological challenges include 1) withstanding power densities on the order of 10 MW/cm^2, 2) accurately positioning optical devices (ideally within ±50 µm) relative to a reference plane, 3) intercepting and accurately profiling high-power beams at incidence angles up to 20° off-normal, 4) accurately measuring beams that are scanned significantly faster than 1 m/s, and 5) measuring highly-dynamic, non-Gaussian beam profiles (beam shaping). This paper describes measurement approaches, challenges, and future research directions for metal AM beam metrology. Preliminary results of laser directed energy deposition experiments illustrate the importance of accurately quantifying PDDs.

Peer-review under responsibility of the international review committee of the 13th CIRP Conference on Photonic Technologies [LANE 2024]

Keywords: laser-based additive manufacturing; power density distribution metrology; beam shaping

1. Introduction

The majority of laser-based additive manufacturing (LBAM) machines operate with a circular, Gaussian power profile with total power up to approximately 1 kW. However, the effect of different power profiles in LBAM is an emerging topic [1]. Alternatives to the circular, Gaussian power profile that have been studied for LBAM include elliptical Gaussian, Bessel, top-hat, and inverse Gaussian (i.e., annular, donut) [1]. These different shapes expand the process space for LBAM and come with a variety of advantages over circular, Gaussian power profiles. Advantages include reduction of spatter [1], reduced powder denudation zone [2], faster build rates, a wider process window [3], reduced porosity [4], reduced thermal gradients [4], and microstructure control [5]. Characterizing the

Nomenclature

1D	1-dimensional
2D	2-dimensional
AM	Additive manufacturing
FPA	Focal plane array
LBAM	Laser-based additive manufacturing
L-DED	Laser directed energy deposition
L-PBF	Laser powder bed fusion
ND	Neutral density
PDD	Power density distribution
RSS	Root sum square
WFPA	Windowless focal plane array

2212-8271
Peer-review under responsibility of the international review committee of the 13th CIRP Conference on Photonic Technologies [LANE 2024]
10.1016/j.procir.2024.08.215

quality of these different power profiles and their relations to the process performance is an unsolved problem.

The laser beam power profile at the working plane and the full beam caustic can be measured with several methods. Ideally, this is done while operating the laser under conditions similar to the AM process (i.e., under high power). The most straightforward way to measure the power profiles is with camera-based methods because they capture the profile with the fewest assumptions. According to T.S. Ross [6], camera-based methods are also the most fully described test method in ISO-11146 for measuring common beam quality metrics [6]. For camera-based methods, this requires a beam splitter to reduce power delivered to the camera. In order to determine the beam waist relative to the building plane, the optical path length needs to be calibrated and referenced to the build platform. The resolution is limited by the camera pixel pitch on the order of a few micrometers. This method was selected for this study.

Other methods include spinning-disc and patterned-glass beam sampling. The spinning disc method uses a tip with a pinhole to sample a small portion of the beam, and the resolution is limited by the pinhole size (e.g., 20 µm) [7]. This may not be suitable for non-Gaussian beams with small features sizes or even circular, Gaussian beams less than 100 µm in diameter [7]. The patterned glass approach measures a scanning laser (i.e., time series signal) and works to deconvolve the time series based on the pattern on the glass and the beam profile [8]. This method works well for off-normal beams as a 1-dimensional (1D) profile measurement; however, the assumptions in the analysis may be a limiting factor for more complicated power density distributions (PDDs).

In this work, we develop and demonstrate a camera-based approach to sampling the high-power laser beam of a powder - blown laser directed energy (L-DED) machine. Results reported here show profile of a nominally Gaussian beam (with minimal ring beam power) as well as the other extreme laser setting of 90 % ring beam power with 10 % core beam power.

2. Methods

2.1. Metrological concept

As described previously, a beam profiler based on beam splitters works by splitting off a small fraction of the beam power for imaging by a focal plane array (FPA). In this case, a commercial double splitter device is implemented wherein each splitter samples approximately 1 % of the incident optical flux so that approximately 0.01 % of the beam flux is reflected onto the imager.

Because the beam splitter device operates on the principle of reimaging a small fraction of the beam flux, the optical path distance from the first beam splitter to the FPA must be equivalent (or as accurate as practical) to the distance from the first splitter to the build plane. The optical path distance calibration approach used in this work is based on locating the position of maximum contrast relative to a reference plane. The contrast source (illustrated in Fig. 1) used for calibration was projected at a central wavelength of 850 nm. At this shorter waveband, the beam splitters are much more reflective than at the laser wavelength of 1070 nm, thus allowing for use of a low power (approximately 1 W) light emitting diode for calibration. The contrast source was imaged through a 125 mm focal length lens at 1× magnification.

Fig. 1 summarizes the optical path distance calibration concept. First, a windowless focal plane array (WFPA) is positioned near the focus of the contrast source. A WFPA is specifically chosen to eliminate refractive elements that would affect: 1) the measured location of the sensor via a laser distance finder, and 2) the perceived maximum contrast location of the imager. The location of maximum contrast (focal plane) then indicates the precise physical location of a sensor (reference plane). The second step is to use the same approach to locate the focus position of the projected image through the beam splitters to match (as accurately as practical) the optical path distance from the first beam splitter to the build plane. Finally, the laser can be profiled in situ.

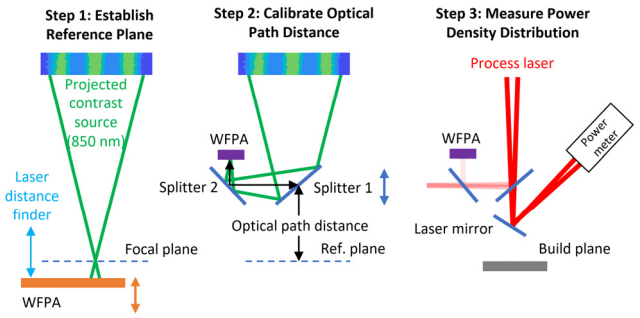

Fig. 1. Steps to optical path distance calibration and beam profiling.

2.2. Image processing

Fig. 2 shows typical data used to locate the maximum image contrast. The position-depended contrast (averaged trough values divided by averaged peak values) is calculated by first finding a set of illuminated contrast bars (illustrated in Figure 2) that exhibit a peak contrast of ≈ 0.6. The signal profile is then calculated by averaging the signal from ten adjacent rows of pixels through five consecutive image frames that cross-section the contrast bars. The contrast is then determined by averaging and ratioing the peak and trough values of the cross-sectional profiles. Finally, a second-order polynomial curve fit is applied to the data, with the peak curve fit value locating the maximum contrast, and therefore the focus.

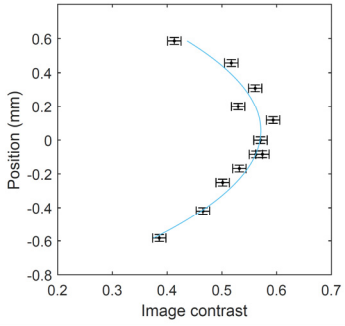

Fig. 2. Example of contrast value as a function of position.

2.3. Measurement uncertainties

The WFPA position uncertainty is based on experience with repeatability of positioning the sensor relative to the reference plane (Type B), estimated to be ±20 µm (k = 1). The contrast uncertainty bars are based on the spatial and temporal nonuniformity of the image sequence, similar to that described in Deisenroth et al. [9]. The root-mean squared error of the mage contrast (horizontal axis of Fig. 2) polynomial curve fit was found to be 0.019. This value of contrast uncertainty corresponds to position uncertainty component of ±145 µm (Type A, k = 1). Root sum squared (RSS) with the initial positioning uncertainty results in a combined focal position measurement uncertainty of ±147 µm.

Step 2 of Fig. 1 introduces the positioning uncertainty for a second time as the first beam splitter is located relative to a reference plane on the splitter device. Thus, the positioning uncertainty of the imager to the reference plane is RSS with the first position uncertainty for a combined optical path distance measurement uncertainty of ±207 µm. Finally, a positioning measurement uncertainty is incurred when the device is installed in the L-DED machine, which is an additional uncertainty (Type B) estimated to be ±25 µm. This results in

combined positioning measurement uncertainty of ±210 µm. This positioning uncertainty corresponds to a nominal beam diameter measurement uncertainty component of less than ±2 µm (Type A, k = 1) due to optical path distance measurement uncertainty for this application. Further evaluation of PDD measurement uncertainty components will be the focus of future work.

2.4. Device implementation

In implementation of the measurement device, two nonidealities were introduced to the conceptual design. The first was due to the low clearance distance from the beam output (with the powder nozzle removed) requiring the use of a bodyless (board-level) camera. Such a camera is not available in windowless form, which therefore introduced a refractive window into the optical path. The implemented imager had a pixel pitch of 2.0 µm which is approximately 25× smaller than the smallest expected feature size of the PDD.

Attenuation of only 99.99 % of the laser power was insufficient to avoid saturating (or damaging) the imager, requiring the introduction of a neutral density (ND) filter, which is a second refractive element. The calibration was performed with both refractive elements in place. It is quite reasonably assumed that the refractive index of the two refractive elements is nearly identical at the calibration wavelength (850 nm) and the laser wavelength (1070 nm) because this is the case for most optical glass used in these applications.

2.5. Evaluation of thermal effects

The L-DED system used in this study has a simplistic optical system, similar to those used in laser welding. After the collimator, a static 90° mirror directs the beam through a single lens and finally through a protective window. As described previously, the measurement device introduces two additional beam splitters and then a ND filter before the beam reaches the detector. If any one of these optical elements were to perform poorly (absorption and distortion by laser heating), the beam shape and focus position could significantly shift with power level and duration. Several powers and intensities were tested up to 480 W applied continuously for 30 s. In all instances, the beam diameters (D4σ) varied by less than 1 %, which is within the required characterization accuracy.

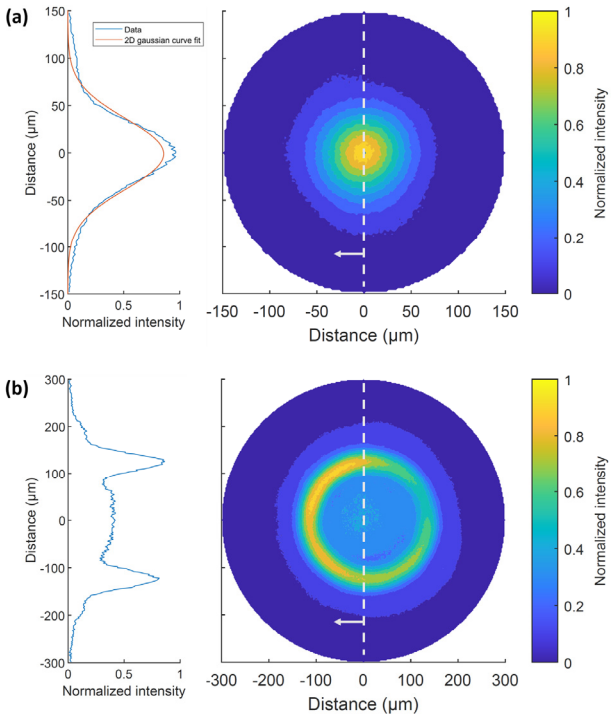

Fig. 3. (a) PDD of the core beam (right) and arbitrary 1D profile (left); (b) PDD of the ring beam with 10 % core beam power (right) and arbitrary 1D profile (left).

2.6. Bead on plate laser scans

Single-track laser scans were conducted with the core beam (Gaussian) and ring beam (90 % ring, 10% core) corresponding to the PDD measurements. The laser power, scan speed, and standoff distance (distance between the nozzle and base plate) were fixed at 226 W (± 5 %), 300 mm/min, and 6 mm. Stainless steel 17-4 powder with a diameter range of 45 µm to 150 µm was used with a fixed hopper disc speed of 15 % and deposited on 1020 steel base plate to produce 15 mm long tracks. Tracks were cross-sectioned perpendicular to the scan direction 1 mm from the end of the track. These were mounted and metallographically prepared for optical microscopy. Bright field images were taken at a total magnification of 100× to reveal the bead morphology.

3. Results

The results reported here show the two extremes of the power ratios available from the laser of this L-DED system: 1) nearly 100 % Gaussian core power, and 2) 10 % core with 90 % ring power. After images were taken under these conditions, the signal levels were simply normalized by the maximum

value of the given distribution. This way, the PDD can be calculated in terms of [W/m^2] from the dimensionless distribution for any power level. Micrographs of bead on plate experiments are also shown for these conditions.

Fig. 3a shows a 2-dimensional (2D) normalized intensity distribution when operating with nearly 100 % of the power applied to the nominally Gaussian core beam. The distribution appears quite circular at intensity values greater than 0.5, but then appears to become more elliptic at lower intensity values.

A 2D bivariate Gaussian curve fit of the distribution exhibited $R^2 = 0.98$, indicating a quite Gaussian distribution, with the minor axis divided by the major axis (ellipticity) value of 0.98. But, the arbitrarily oriented 1D profile through the center of the 2D distribution shows notable variations from an ideal 2D Gaussian distribution—especially the 'wings' that appear at distances of more than ±75 µm from the distribution center, as well as the pointed peak of the distribution.

Fig. 3b shows a highly circular ring shape, but the peak values of the flux from the ring show a significant variation around the circumference. The normalized optical flux around the circumference of the ring decreases from 1.0 to less than 0.6, indicating a 40 % variation in flux in contrast to what should be expected to be a quite uniform distribution. The arbitrary cross-section indicates an average profile that is nominally symmetric at that location, while the core beam at 10 % of the power of the ring reaches a normalized optical flux of approximately 0.5 of the peak flux.

Fig. 4a and 4b show the top view of bead on plate experiments for the core and ring beam PDDs. The core beam shows an instability compared to the ring beam, which produces a continuous bead along the track length. Fig. 4c and 4d show cross-sectional micrographs taken at 1 mm from the end of the tracks. The bead morphologies are similar with a marginally smaller bead height for the ring beam. Additional experiments are required to reliably quantify the differences in bead morphologies. However, it is clear from these initial results that that the process can shift from an unstable regime to a stable regime when changing the PDD.

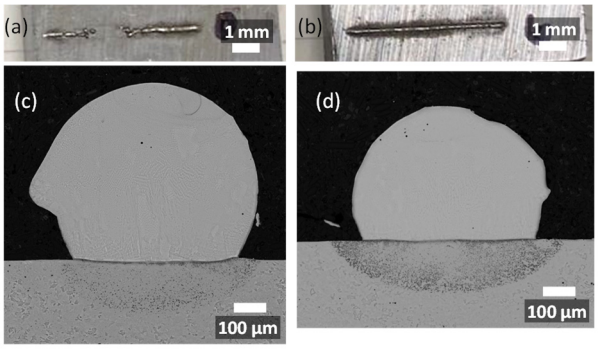

Fig. 4. (a) track top view of core beam, (b) track top view of ring beam with 10 % core beam power, (c) track cross-section of core beam, (d) track cross-section of ring beam with 10 % core beam power.

4. Discussion

Several sources of nonideal beam distributions caused by L-DED machine characteristics have been identified, including 1) nonuniform transmission of light through the ring and core laser fibers, 2) scattering and/or misalignment of the laser optics, and 3) dirtying of the protective laser window. Contamination of the laser window has been ruled out due to the frequency of inspection and cleaning. Additionally, nonuniform transmission from the laser fiber seems unlikely, although this can be tested with similar methods to that used in this work. And so, it appears that axial and/or angular misalignment of the laser optics (collimator, mirror, and/or lens) may be the primary cause of nonideal laser power density distributions.

Additionally, the measurement device may introduce nonidealities into the detection of the laser distribution. Specifically, it has been shown here that the beam splitters reflect approximately 100× more optical flux at 850 nm than at the laser wavelength of 1070 nm. And so, it is currently unknown what proportion of laser pump diode is reflected through the beam splitters at a central wavelength of approximately 930 nm.

5. Conclusions and future work

This work demonstrates the importance of measuring laser PDD in situ—in this case on a modified commercial L-DED machine. When the core beam was operated nominally without the ring beam, it was found that the beam had significant variations from an ideal Gaussian profile, including a pointed peak and 'wings' at ±75 µm from the center. Furthermore, the ring beam exhibited more than 40 % variation in peak flux around its circumference. Both of these variations from an ideal profile may have significant effects on part quality, variability, and reproducibility—however, investigating such specific effects was out of the scope of the current study. Nevertheless, preliminary experimental L-DED bead on plate experiments prove the importance of accurately quantifying beam PDDs. It is shown clearly that a bead deposition process can shift from an unstable regime to a stable regime when changing the PDD.

In order to make these PDD measurements, we developed a beam sampling device that can 1) sample high power beams relevant to metal AM, 2) sample the beam within ±210 µm of the nominal position, 3) accurately measures Gaussian and non-Gaussian (ring and core) beam profiles.

An optical path distance calibration method is detailed in this work, in which a contrast source at an adjacent waveband (centered on 850 nm) to the laser wavelength (centered on 1070 nm) is implemented to leverage the fact that the beam sampler has many orders of magnitude higher throughput at the slightly shorter wavelength. In future work, this distance calibration can be improved by projecting a contrast source with a greater numerical aperture to improve sensitivity to contrast with position.

Future work will also eliminate all refractive elements (ND filters and imager windows) from the optical path of the measurement device to eliminate any assumptions about refractive index. In this future approach, beam attenuation must occur only by reflective optics, while also filtering out any residual light generated by the laser pump diodes at approximately 930 nm. This improved device will be used as a 'standard' to measure beam profiles that will be compared against other devices that are specifically adapted to measuring the remaining PDD measurement challenges.

The remaining challenges that were not addressed in this work include profiling beams that are scanned significantly faster than 1 m/s while also being dynamically shaped. Addressing this challenge will likely require introduction of refractive lenses into the beam sampler in order to uniformly magnify the beam for imaging by high-speed camera, which typically have pixels that are much larger than useful for many metal AM beam profiles (pixel pitch on the order of 20 μm). Measurement of beams at incidence angles up to 20° off-normal may require use of precision gimbals, and/or other beam attenuation or sampling approaches. In any case, these auxiliary devices for highly dynamic and/or off-normal beams will be validated against the 'standard' reflective-only device.

6. Acknowledgements

The authors wish to thank Alkan Donmez for his continued support and review of this research work. The authors also wish to thank Steven Grantham for his intellectual and material support of this work from its conception.

7. References

[1] Wischeropp TM, Wischeropp T. Advancement of selective laser melting by laser beam shaping. Springer; 2021.
[2] Okunkova A, Volosova M, Peretyagin P, Vladimirov Y, Zhirnov I, Gusarov A. Experimental approbation of selective laser melting of powders by the use of non-Gaussian power density distributions. Phys Proc 2014;56:48–57.
[3] Grünewald J, Gehringer F, Schmöller M, Wudy K. Influence of Ring-Shaped Beam Profiles on Process Stability and Productivity in Laser-Based Powder Bed Fusion of AISI 316L. Metals. 2021;11(12).
[4] Tumkur TU, Voisin T, Shi R, Depond PJ, Roehling TT, Wu S, et al. Nondiffractive beam shaping for enhanced optothermal control in metal additive manufacturing. Sci Adv. 2021;7(38):eabg9358.
[5] Shi R, Khairallah SA, Roehling TT, Heo TW, McKeown JT, Matthews MJ. Microstructural control in metal laser powder bed fusion additive manufacturing using laser beam shaping strategy. Acta Materialia. 2020 Feb 1;184:284–305.
[6] Ross TS. Laser beam quality metrics. Tutorial Texts in Optical Eng; 2013.
[7] PRIMES. Original Instructions FocusMonitor FM+ HPD; 2021.
[8] Koglbauer A. More Than Beam Profiling: A new approach for beam diagnostics in 3D additive manufacturing systems. Laser Technik Journal. 2018;15(3):40–4.
[9] David Deisenroth, Sergey Mekhontsev, Brandon Lane, Leonard Hanssen, Ivan Zhirnov, Vladimir Khromchenko, et al. Measurement Uncertainty of Surface Temperature Distributions for Laser Powder Bed Fusion Processes. J of Res of NIST. 2021;126.